



Cite this: *Nanoscale*, 2017, **9**, 1475

Ultrafast carrier dynamics in bimetallic nanostructure-enhanced methylammonium lead bromide perovskites†

Holly F. Zarick,^{a,b} Abdelaziz Boulesbaa,^c Alexander A. Puretzky,^c Eric M. Talbert,^{a,b} Zachary R. DeBra,^{a,b} Naiya Soetan,^{a,b} David B. Geohegan^c and Rizia Bardhan^{*a,b}

In this work, we examine the impact of hybrid bimetallic Au/Ag core/shell nanostructures on the carrier dynamics of methylammonium lead tribromide (MAPbBr₃) mesoporous perovskite solar cells (PSCs). Plasmon-enhanced PSCs incorporated with Au/Ag nanostructures demonstrated improved light harvesting and increased power conversion efficiency by 26% relative to reference devices. Two complementary spectral techniques, transient absorption spectroscopy (TAS) and time-resolved photoluminescence (trPL), were employed to gain a mechanistic understanding of plasmonic enhancement processes. TAS revealed a decrease in the photobleach formation time, which suggests that the nanostructures improve hot carrier thermalization to an equilibrium distribution, relieving hot phonon bottleneck in MAPbBr₃ perovskites. TAS also showed a decrease in carrier decay lifetimes, indicating that nanostructures enhance photoinduced carrier generation and promote efficient electron injection into TiO₂ prior to bulk recombination. Furthermore, nanostructure-incorporated perovskite films demonstrated quenching in steady-state PL and decreases in trPL carrier lifetimes, providing further evidence of improved carrier injection in plasmon-enhanced mesoporous PSCs.

Received 24th October 2016,
Accepted 9th December 2016

DOI: 10.1039/c6nr08347a

www.rsc.org/nanoscale

Introduction

An unprecedented rise in efficiency has been observed in methylammonium lead trihalide (MAPbX₃, X = I, Cl, Br) perovskite solar cells (PSCs) from 3.8% in 2009 to >20% in early 2016.^{1–5} The inexpensive materials and low cost of solution-based processing⁶ make this class of perovskites amenable to scalable manufacturing and has the potential to be a serious contender for utility-scale solar power. MAPbI₃-based PSCs have been a primary focus due to their near-complete visible light absorption in films <1 μm and their fast charge extraction rates.^{7,8} However, the poor stability of MAPbI₃ and rapid degradation in humidity has remained a major obstacle for commercialization,^{9,10} necessitating complex encapsulation techniques.¹¹ MAPbBr₃ is a promising alternative to MAPbI₃ with a large 2.2 eV bandgap, which gives rise to a high open circuit voltage ($V_{oc} \sim 1.2\text{--}1.5\text{ V}$)^{12,13} and makes it an ideal material for

tandem devices. Their long exciton diffusion length (>1.2 μm) enables good charge transport in devices.¹⁴ In addition, MAPbBr₃ demonstrates higher stability towards air and moisture due to its stable cubic phase and low ionic mobility relative to the pseudocubic MAPbI₃, in which inherent lattice strain provides an avenue for increased diffusion.^{11,14–16} However, a relatively large exciton binding energy, E_B , (76 meV) and poor light absorption beyond its band edge at 550 nm has limited the efficiencies for MAPbBr₃ solar cells.^{11,15,17,18}

Metal nanostructures provide an effective route to improve light harvesting in solar cells, enhance optical absorption, and increase carrier generation, resulting in higher efficiency.¹⁹ The localized surface plasmon resonances (LSPRs) supported by metal nanostructures simultaneously give rise to intense electromagnetic near-fields and light scattering in the far fields,^{8,2} which have been harnessed to enhance the performance of both planar^{20–22} and mesoporous solar cells.^{23–27} Recent work on plasmon-enhanced PSCs has suggested that in addition to improved scattering and near field coupling, metal nanostructures also reduce the exciton binding energy (E_B) and enable better charge separation.^{28–31} Highly polarizable metal nanostructures have also been shown to favor radiative decay processes, increasing the optical path length of incident photons by the reabsorption of emitted radiation within the perovskite absorber layer.³² Additionally, by controlling the position and polarization of metal nanostructures, the result-

^aDepartment of Chemical and Biomolecular Engineering, Vanderbilt University, Nashville, TN 37235, USA. E-mail: rizia.bardhan@vanderbilt.edu

^bDepartment of Mechanical Engineering, Vanderbilt University, Nashville, TN 37235, USA

^cCenter for Nanophase Materials Sciences, Oak Ridge National Laboratory, Oak Ridge, TN 37831, USA

†Electronic supplementary information (ESI) available. See DOI: 10.1039/c6nr08347a

ing LSPR modes can couple with the perovskite and give rise to strong light-matter interactions at the metal/perovskite interface.³³ In our previous work, we demonstrated the use of bimetallic gold/silver core/shell nanostructures (Au/Ag NSs) for enhancing the performance of organic photovoltaics²² as well as dye-sensitized solar cells.²³ Here we investigate the interactions of Au/Ag NSs with MAPbBr₃ perovskites in the mesoporous device architecture. The engineered shape and controlled composition of the Au/Ag NSs gives rise to panchromatic light absorption, and their sharp edges and corners result in intense electric fields attributable to the quasistatic lightning-rod effect.^{34–37} These spectral characteristics of Au/Ag NSs result in broadband light absorption above the band edge of MAPbBr₃, a phenomenon useful for device performance. We integrated Au/Ag NSs within the mesoporous TiO₂ layer of MAPbBr₃ PSCs, examined the device performance, and correlated these trends with the carrier dynamics of MAPbBr₃ with both transient absorption spectroscopy (TAS) and time-resolved photoluminescence (trPL). Our results demonstrate that carrier lifetimes significantly decrease for both TAS and trPL in the presence of the bimetallic nanostructures. The enhancements observed in the presence of Au/Ag NSs in both photocurrent and incident photon to charge conversion efficiency (IPCE) of MAPbBr₃ PSCs correlate well with the decrease in carrier lifetimes. We attributed these effects in carrier dynamics to enhanced photoinduced charge generation and rapid electron injection into TiO₂ in the presence of the plasmonic nanostructures, as well as reduced recombination and improvement in hot carrier thermalization in the perovskite.

Experimental methods

All reagents were purchased from Sigma Aldrich unless otherwise specified and were used as received without further purification. All the H₂O used for substrate preparation and nanostructure synthesis was ultrapure H₂O (18.2 MΩ) obtained from a Milli-Q Direct-Q 3UV system. All work done under an inert atmosphere was conducted in a nitrogen filled MBraun LabStar glovebox (<0.5 ppm O₂).

Au/Ag nanostructure synthesis

Au/Ag nanostructures were synthesized following a procedure described in our previous work.³⁸ Au nanocube cores were prepared following a seed-mediated growth method in which Au seeds were formed by adding 600 μL of ice cold, freshly prepared 10 mM NaBH₄ to a solution containing 7.5 mL of 100 mM CTAB, 2.75 mL H₂O, and 0.8 mL of 10 mM HAuCl₄. The solution was stirred vigorously for 1 minute before being transferred to a 35 °C water bath where it was left to stay for one hour. The seeds were then diluted by a factor of 10 with water before being added to a growth solution composed of 6.4 mL of 100 mM CTAB, 0.8 mL of 10 mM HAuCl₄, and 3.8 mL of 100 mM ascorbic acid that were added sequentially to 32 mL of ultrapure H₂O. Post-Au seed addition, the mixture was mixed by gentle inversion, and then left to react un-

disturbed for 5 hours in a 35 °C water bath. A ligand exchange was performed on the Au NC cores before Ag layer growth was performed: Au NCs were centrifuged at 1100 RCF for 15 minutes in 7.5 mL aliquots, the supernatant was removed, and the particles were washed and soaked in 3.75 mL of 20 mM CTAC for 15 minutes. This was repeated for a total of 3 spins and two 15 minute soaks. The final CTAC-capped Au NC pellet was redispersed in 500 μL of water to make the final precursor solution for Au growth. Typically, 400 μL of the Au NC precursor was added to 10 mL of 20 mM CTAC along with 100 μL of 10 mM KBr. This was mixed by inversion and heated in a 65 °C water bath for 10 minutes before adding into 100 μL of 10 mM AgNO₃ and 300 μL of 100 mM ascorbic acid, mixing again by inversion, and placing it back in the 65 °C water bath for two hours.

Silica-coating of Au/Ag nanostructures

Au/Ag NSs were capped with a thin ~4 nm layer of silica by modifying a previously described procedure.³⁹ In a 50 mL round bottom flask, 30 mL of as-prepared Au/Ag NSs were first functionalized with 400 μL of a freshly prepared 1 mM 3-aminopropyltrimethoxysilane (APTMS) solution for 15 minutes at room temperature while stirring at ~500 RPM. A 0.54 wt% solution of sodium silicate was adjusted to pH ~10.2 with 5 N HCl followed by injecting 500 μL into the APTMS-functionalized Au nanocubes. The reaction mixture was stirred for 3 minutes at room temperature and then transferred to a 50 °C oil bath and stirred for 4.5 hours to form the uniform silica shell. The reaction was quenched by placing the coated nanostructures in the fridge overnight. The particles were then centrifuged at 900 RCF (×2) and washed once with water prior to imaging and device incorporation.

Perovskite Layer Fabrication

MAPbBr₃-sensitized layers were deposited on either glass for TAS and PL testing or FTO-glass for full device characterization, including JV and IPCE testing. Glass and FTO-glass substrates were cleaned by sonication for 30 min in a 2 vol% solution of Hellmanex in H₂O, rinsed first with H₂O and then IPA, and then sonicated for an additional 15 minutes in a 1 : 1 v/v mixture of IPA/acetone. The substrates were then rinsed with IPA, dried with N₂, and plasma treated for 15 minutes immediately before use. A ~50 nm layer of compact TiO₂ was deposited on the substrates by hydrolyzing 40 mM TiCl₄ at 70 °C. The substrates were removed from the TiCl₄ bath after one hour, rinsed with H₂O and EtOH, dried with N₂, and then annealed at 500 °C for 15 minutes. Mesoporous TiO₂ was deposited by spin coating a diluted solution of 18NRT Dyesol paste (1 : 2 : 1 by weight of EtOH : α-terpineol : Dyesol) at 2500 RPM for 60 seconds, dried on a 100 °C hot plate, and then sintered at 500 °C for 30 minutes. Plasmon-enhanced samples were prepared in the same manner; however, washed and concentrated pellets of silica-coated Au/Ag NSs were added directly to the diluted Dyesol paste to the desired concentrations and mixed until homogeneous before spin coating. All mesoporous layers received a 40 mM TiCl₄ post-treatment at 70 °C for 30 minutes, were rinsed with H₂O and EtOH, dried with N₂,

and fired in air at 500 °C for 15 minutes. At this point, all mesoporous TiO₂ substrates were transferred into an inert environment. MAPbBr₃ films were then prepared following a modified two-step sequential deposition process.⁴⁰ First, a 1 M solution of PbBr₂ in DMF was stirred on a 75 °C hot plate for 20 minutes and filtered with a 0.45 μm PTFE filter immediately before use. TiO₂ substrates were heated to 75 °C prior to spin-coating 200 μL of the filtered PbBr₂ solution at 2500 RPM for 60 seconds followed by a 30 minute annealing at 75 °C. Once cooled post-annealing, the substrates were dipped in IPA for 1–2 s before being placed in a heated (50 °C) solution consisting of 15 mg mL⁻¹ MABr (Dyesol) in IPA for 10 minutes, rinsed with IPA, and annealed again at 75 °C for 30 minutes.

PSC fabrication

Full devices were fabricated on FTO-sensitized substrates following a typical fabrication process.⁴¹ An HTM was prepared by the addition of 72.3 mg of SpiroMeOTAD (2,29,7,79-tetrakis (*N,N*-di-*p*-methoxyphenylamine)-9,9-spirobifluorene, EMD), 29 μL of 4-*tert*-butylpyridine, 18 μL of a 520 mg mL⁻¹ LiTFSI (lithiumbis(trifluoromethylsulfonyl)imide) in acetonitrile solution, and 29 μL of a 300 mg mL⁻¹ tris(2-(1*H*-pyrazol-1-yl)-4-*tert*-butylpyridine)cobalt(III) bis(trifluoromethylsulfonyl)imide (Lumtec) in acetonitrile solution to 1 mL chlorobenzene.⁴¹ 100 μL of the HTM solution was then deposited on top of MAPbBr₃-sensitized TiO₂ films at 3000 RPM for 30 s. The samples were left overnight in darkness and dry air before 80 nm Au contacts were deposited *via* thermal evaporation in 8 mm diameter circles utilizing shadow masks in an Angstrom Amod system.

Materials characterization

All optical absorbance spectra were taken using a Varian Cary 5000 UV-vis NIR spectrophotometer. Scanning and transmission electron microscopy were conducted with a Zeiss Merlin and an FEI Tecnai Osiris, respectively. Characterization of power conversion performance of full device PSCs was conducted with a Newport solar simulator and a Metrohm potentiostat. Each cell received 1 sun (100 mW cm⁻²) of power from the solar simulator at AM 1.5 over equivalent areas of 0.081 cm² and was tested at a scan rate of 50 mV s⁻¹. An average of 10 devices were tested for each sample type. Incident photon conversion efficiency (IPCE) measurements were conducted with a 6 W Fianium fiber laser supercontinuum source coupled with a Fianium acousto-optic tunable filter to filter out the desired excitation wavelength from the white light source.

Transient absorption measurements

Femtosecond transient absorption measurements were conducted using a home-built pump-probe setup based on a femtosecond laser system that utilizes seed pulses from a titanium sapphire oscillator (Micra, Coherent), amplified by a Ti:Sapphire amplifier (Legend USP-HE, Coherent) to provide 800 nm femtosecond pulses (2.5 mJ per pulse) operating at a 1 kHz repetition rate with ~45 fs pulse durations. The Legend amplifier is pumped by using a Nd:YLF laser (Evolution-30, Coherent). A small portion of the output of the amplifier

(~4 μJ per pulse) is focused on a sapphire window (2 mm thick) to generate a white light continuum (WLC) probe (450–900 nm). To minimize temporal chirp in the spectrally broad WLC probe, a set of parabolic mirrors was used to collimate and focus the WLC on the sample. The transmitted probe was focused onto 100 μm core fiber coupled with a spectrometer/CCD (USB2000ES, Ocean Optics). The pump pulse at 400 nm is generated by doubling ~50 μJ per pulse of the 800 nm fundamental in a BBO crystal. The pump beam passes through a delay-line to allow control of time-delay between the pump and the probe. In order to measure the absorbance changes between every two successive laser shots, the pump beam was chopped at a frequency of 500 Hz. At the sample, the spot sizes of the pump and probe pulses were 100 μm and 50 μm, respectively. The pump energy fluence at the sample was ~5 μJ cm⁻².

Photoluminescence measurements

The photoluminescence (PL) spectra were recorded using a spectrometer (Acton SP2300) equipped with a CCD (Princeton Instruments, Pixis 256), which was coupled to a microscope. The time-resolved PL spectra were recorded by using a time correlated single photon counting (TCSPC) module (Horiba Scientific with Picosecond Photon Detection Module, PPD-850 and Fluorohub model: Horiba JY IBH). The PPD-850 was mounted to a second port of the same spectrometer. MAPbBr₃-sensitized TiO₂ films, with and without Au/Ag NSs, were excited at 400 nm using a second harmonic signal of a Ti:sapphire laser (Coherent, Mira 900, 5 ps pulse length, 76 MHz repetition rate). To match TCSPC requirements, the laser repetition rate was reduced to ~5 kHz using a pulse picker (Coherent). The output from the pulse picker was frequency doubled using an ultrafast harmonic generator (Coherent 5-050) and directed into a microscope to illuminate the films through a 100× microscope objective (beam spot size ~1 μm). All films were initially exposed to 400 nm light for ~20 min in order to stabilize the samples.

Results and discussion

The MAPbBr₃ PSCs were fabricated by infiltrating the perovskite within a ~500 nm mesoporous titania (mp-TiO₂) layer following a modified two-step sequential deposition process (see Experimental methods for details).⁴⁰ The mp-TiO₂ provides an ideal scaffold for perovskite crystal growth and for embedding the bimetallic nanostructures, and provides a pathway for selective charge collection.^{42,43} The incorporated Au/Ag NSs were synthesized following a seed-mediated growth method described in our previous work.³⁸ The NSs were coated with a conformal ~5 nm layer of silica (silica-coated Au/Ag NSs, Fig. 1c), then homogeneously mixed throughout the mesoporous TiO₂ layer (Fig. 1a) allowing close proximity of the NSs to the MAPbBr₃ crystals to enable plasmonic enhancement. The silica minimizes charge recombination at the perovskite/nanoparticle interface by prohibiting direct conduction of

plasmon electrons into the perovskite. It also prevents Ostwald ripening during the high temperature TiO_2 annealing processes, and avoids degradation of the NSs by the halide ions in the perovskite.^{23,24,32} The color-enhanced cross-sectional SEM image shown in Fig. 1b (non-color modified in the ESI, Fig. S2†) depicts the relative morphology and layer thicknesses of the MAPbBr_3 PSCs. The representative TEM images of Au/Ag NSs shown in Fig. 1c (silica-coated) and Fig. S1† (without silica coating) illustrate the two distinct geometries that form during synthesis, nanocubes and nanopyramids, with distinct plasmon

resonances centered at 540 nm and 615 nm correlating with the two geometries, respectively (Fig. 1d). The two absorbance peaks of the mixed NSs promote light scattering above the bandgap of MAPbBr_3 as well as provide complementary broadband absorption spanning the entire visible spectrum.

The light harvesting ability of the Au/Ag NSs within the MAPbBr_3 PSCs was probed by comparing the absorbances of reference, MAPbBr_3 -sensitized TiO_2 films without nanostructures, to $\text{TiO}_2/\text{MAPbBr}_3$ mesoporous films containing two different densities of silica-coated Au/Ag NSs, 0.5 wt% and 1.0 wt% (Fig. 2a). An increase in absorbance was observed with the increasing nanostructure density in the 410–540 nm spectral range where the plasmon resonances of the bimetallic nanostructures overlap with the absorption of the MAPbBr_3 perovskite. This indicates enhanced radiative light trapping in the photoactive layer as a result of the Au/Ag NSs. While changes in absorbance above 550 nm are subtle, detailed analysis of relative absorbance enhancement (Fig. S3a†) demonstrates that Au/Ag NSs promote broadband light absorption complementary to where MAPbBr_3 absorbs light. The absorption enhancement we observed experimentally in our work is comparable to the theoretical enhancements predicted for perovskite active layers embedded with plasmonic metal nanoparticles.⁴⁴ However enhancement in solar cells is driven by several different factors that collectively determine the external quantum efficiency and ultimately influences the total power conversion efficiency. These include the photon absorption efficiency (η_{abs}) which is the ratio of absorbed light to incident light, the exciton dissociation efficiency (η_{diss}) which is the ratio of photoexcited excitons that are converted to free carriers, the charge carrier transport efficiency (η_{ct}) which is the ratio of the generated free carriers that reach the electrode prior to recombination, and charge collection efficiency (η_{coll}), the ratio of carriers that are collected after the final interface between the active layer and the electrodes.²² The contribution from each of these factors was examined by evaluating the device efficiencies. We investigated the device performance of the PSCs by comparing the power conversion efficiencies

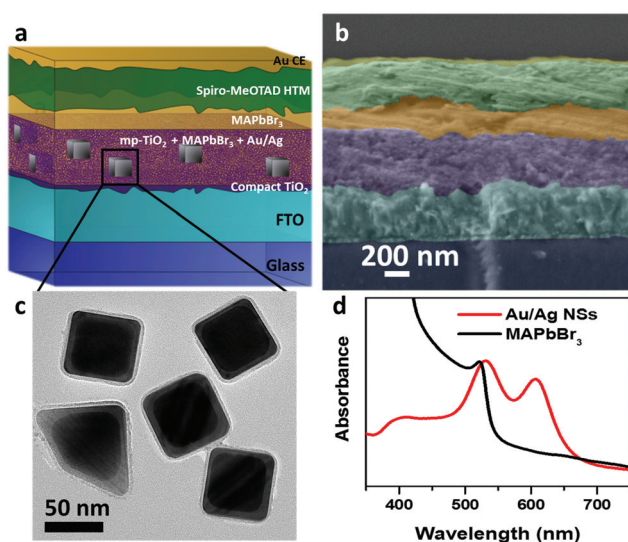


Fig. 1 (a) Schematic representation of a MAPbBr_3 perovskite solar cell integrated with bimetallic Au/Ag nanostructures. The nanostructures are not shown to scale in the mesoporous TiO_2 layer. A cross-sectional SEM image of a representative reference device with an Au counter electrode (CE) is shown in (b). Coloring of the layers has been added for clarity. (c) TEM image of the bimetallic nanostructures coated with a conformal ~ 5 nm layer of silica. The normalized absorption spectrum of MAPbBr_3 -sensitized TiO_2 films compared to the normalized extinction spectrum of the Au/Ag NSs is shown in (d); spectra are normalized to the peaks at 530 and 535 nm, respectively.

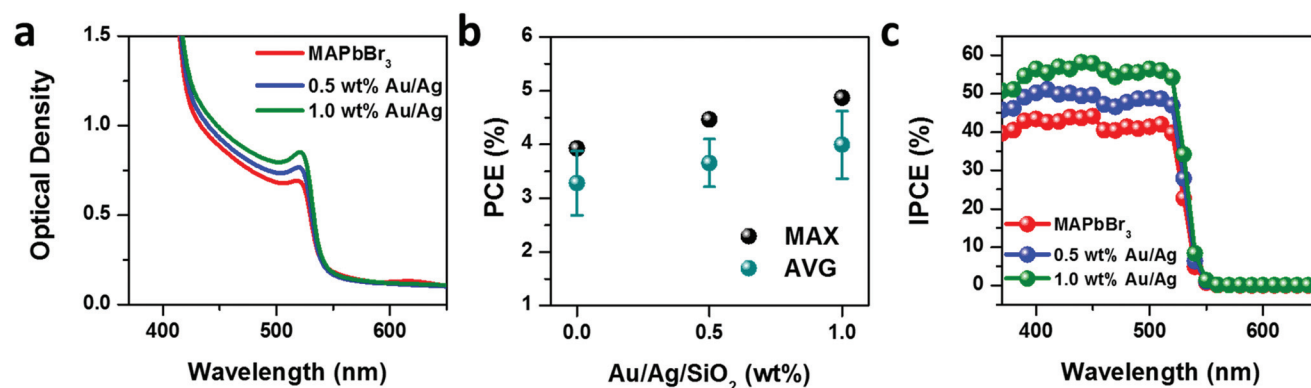


Fig. 2 (a) Optical absorption spectra of mesoporous TiO_2 infiltrated with MAPbBr_3 and integrated with varying concentrations of silica-coated Au/Ag nanostructures. (b) The best and average power conversion efficiencies of devices as a function of varying concentrations of Au/Ag nanostructures (wt%). Error was calculated from standard deviations of ~ 10 devices tested at each concentration. (c) IPCE of the same devices as a function of excitation wavelength.

(PCE's) of full reference MAPbBr₃ PSCs with the plasmon-enhanced devices containing both 0.5 and 1.0 wt% silica-coated Au/Ag NSs (Fig. 2b). Average values and standard deviation for PCE were calculated from ~10 devices for each reference, 0.5 wt% Au/Ag, and 1.0 wt% Au/Ag-incorporated devices. A steady increase in PCE is observed for both 0.5 and 1.0 wt% silica-coated Au/Ag NS incorporations, with the best PCEs measured at 4.5% and 4.9% respectively, compared to the reference devices of 3.9% efficiency. The device parameters, Fig. S4,† show that the measured 26% increase in efficiency with Au/Ag nanostructures is not only attributed to an increase in the short circuit current density, J_{sc} , correlated with η_{abs} and η_{diss} , but also the fill factor (FF) and open circuit voltage (V_{oc}) correlated with η_{ct} and η_{coll} . This suggests that the nanostructures improve light harvesting in the devices, as well as increase charge transfer and reduce carrier recombination. However further improvements in η_{abs} , η_{diss} , η_{ct} , and η_{coll} collectively could potentially result in higher overall efficiencies in both reference and plasmonic devices.

While several studies have focused on plasmonic enhancement of PSCs,^{28,29,31,32,45–48} the carrier dynamics in metal nanostructure-incorporated PSCs remain poorly understood. Here we have employed a combination of TAS and trPL to understand the carrier dynamics in MAPbBr₃ reference films (non-enhanced) and investigate the impact on the exciton generation and charge recombination in MAPbBr₃ in the presence of Au/Ag NSs. TAS studies were performed on films of MAPbBr₃-infiltrated in the mp-TiO₂ layer with a compact-TiO₂ electron acceptor layer (without SpiroMeOTAD). The samples were pumped at 400 nm to fill the perovskite conduction

band, and the resulting absorption dynamics were probed with a white light continuum from 450 to 600 nm. The TA spectra of mp-TiO₂/MAPbBr₃ (Fig. 3a) show a ground state bleaching signal at 530 nm near the band edge of MAPbBr₃ as the valence band electrons are excited to the conduction band by the pump pulse.⁴⁹ A weak photoinduced absorption (PIA) signal at 490 nm is also observed, which is a result of stimulated absorption above the saturated conduction band states.⁵⁰ Our TA evolutionary spectra are in good agreement with those reported in the literature for MAPbBr₃.^{51,52} The normalized decay of the PIA band at 490 nm (Fig. 3b) and dynamics of the photobleach (PB) at 530 nm (Fig. 3c) were fit with a triexponential function yielding both a fast (τ_1) and a slow (τ_2) decay component as well as an initial rise time (τ_R) related to PIA/PB band formation. The amplitudes (A), time constants (τ), and amplitude-weighted carrier lifetimes derived from the fits are listed in Table 1 (530 nm PB dynamics) and Table SI† (490 nm PIA dynamics). The bleach formation kinetics in MAPbBr₃ result from the relaxation of hot electron-hole pairs from the high excited states to quasi-thermal equilibrium states, which gives rise to state-filling of the conduction band, a phenomenon contributed by longitudinal optical phonon scattering.^{52,53} The decay kinetics result from the relaxation of the conduction band population by recombination and charge transfer to TiO₂. Here τ_1 is attributed to phonon scattering and trap-assisted recombination, and τ_2 is contributed by electron injection into the TiO₂.^{8,52}

To understand the effect of plasmonic nanostructures on the carrier dynamics of MAPbBr₃-infiltrated mp-TiO₂ films, the TA evolutionary spectra were recorded with 0.5 wt% and

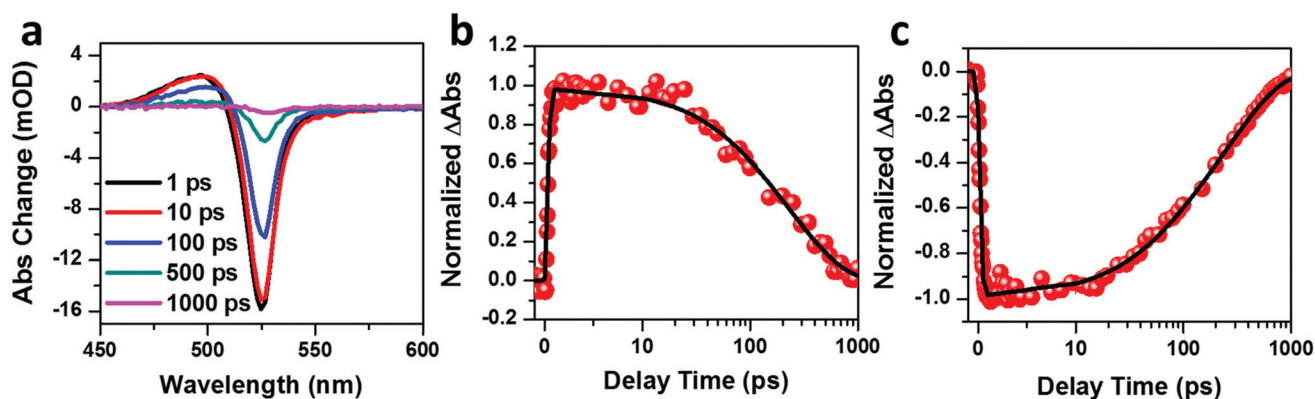


Fig. 3 (a) Transient absorption spectra at various time delays of a mesoporous TiO₂ film infiltrated with MAPbBr₃. Decay kinetics at 490 nm and 530 nm are shown in (b) and (c), respectively, with the experimental data (symbols) fitted with a triexponential decay function (smooth lines). Early time scales are plotted linearly; later time scales (>10 ps) plotted on a base-10 logarithmic scale.

Table 1 Amplitudes (A), time constants (τ), and amplitude-weighted lifetimes (τ_{avg}) derived from triexponential fits of the transient absorption for the different samples at the photobleach band located at 530 nm

Sample	τ_R [ps]	A_1	τ_1 [ps]	A_2	τ_2 [ps]	τ_{avg} [ps]
MAPbBr ₃	0.20 ± 0.02	-0.23 ± 0.06	57 ± 16	-0.76 ± 0.06	312 ± 21	253
0.5 wt% Au/Ag	0.09 ± 0.03	-0.29 ± 0.06	39 ± 10	-0.64 ± 0.07	225 ± 20	167
1.0 wt% Au/Ag	0.15 ± 0.01	-0.44 ± 0.01	25 ± 2	-0.55 ± 0.01	168 ± 6	104

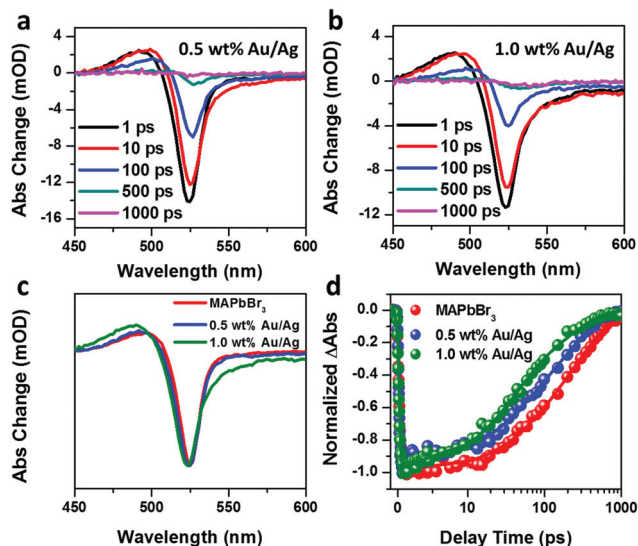


Fig. 4 Transient absorption spectra at various time delays of mesoporous $\text{TiO}_2/\text{MAPbBr}_3$ and those containing 0.5 wt% (a) and 1.0 wt% (b) of silica-coated Au/Ag NSs. Normalized TA spectra at the maximum bleach peak (~ 1 ps time delay) comparing the reference and the Au/Ag NS-enhanced samples are shown in (c). (d) Decay kinetics at 530 nm for the reference and Au/Ag NS-incorporated samples. Decay kinetics are shown with the experimental data (symbols) fitted with a triexponential decay function (smooth lines). Early time scales are plotted linearly; later time scales (>10 ps) plotted on a base-10 logarithmic scale.

1.0 wt% Au/Ag NSs (Fig. 4a and b). Whereas the peak positions of the PB state of the Au/Ag NS-incorporated samples are comparable to that of the reference (Fig. 3), the bandwidth of the PB increases with the increasing particle density of NSs. The broadening of the PB state may be attributed to a more rapid band filling in the nanostructure-incorporated films relative to the reference films. Sharma *et al.*⁵¹ observed a similar phenomenon in MAPbBr_3 thin films with increasing pump energy fluence as higher carrier densities result in a saturation of conduction band levels near the bandgap. This is also supported in our data from the decreasing maximum bleach amplitude with the increasing particle density (Fig. 3a and 4a, b), as more rapid thermalization would lead to less optimization of energy states. It is also possible, however, that the broadening may be attributed to the formation of trap states. In the TA spectra of perovskites, trap states are characterized by a weak bleach absorption with a broad distribution that decays red-shifted, or below the energy, of the optical band gap of the perovskite.⁵⁴ These trap states have longer decay times than the PB state and are populated by the relaxation of hot carriers and can result in the blocking of weakly allowed transitions during excitation.⁵⁵ While the weak sub-bandgap bleach of the 1.0 wt% sample identifies some trap-state filling, the peak broadening more strongly indicates an increased rate of electron–phonon coupling. The enhanced PCE of devices (Fig. 2) at these concentrations supports this hypothesis as the collection of free carriers is enhanced. Trapped excitons have higher exciton binding energies (E_B),⁵⁵ decreasing the prob-

ability of exciton dissociation and increasing the probability of recombination, manifesting as decreased efficiency in the solar cells. Since plasmonic nanoparticles have been reported to lower the E_B (or induce resonant energy transfer to enable exciton dissociation),^{29–31} the observed increases in photocurrent for plasmon-enhanced PSCs likely stem from a combination of electromagnetic effects and reduced E_B .

The recoveries of the PB at 530 nm were normalized and fit with a triexponential decay function for all samples (Fig. 4d); the amplitudes and lifetimes derived from the fits are shown in Table 1. The carrier dynamics at 490 nm are provided in the ESI (Fig. S5 and Table S1†). We first compared the bleach formation time, τ_R , between the reference and the plasmon-enhanced samples, which has been attributed to the thermalization of hot carriers after photoexcitation.^{56,57} During thermalization in MAPbBr_3 , optical hot phonons are generated by the coupling of phonons with hot electrons that subsequently slows the cooling of carriers and increases the τ_R .⁵² In MAPbBr_3 systems, this phenomenon has been termed the ‘hot phonon bottleneck effect’.^{58,59} As seen in Table 1, both plasmon-enhanced samples, containing 0.5 and 1.0 wt% silica-coated Au/Ag NSs, exhibit faster thermalization times compared to the reference MAPbBr_3 . This faster τ_R lifetime likely results from plasmon–phonon coupling between the nanostructures and the perovskite which limits the coupling of phonons with hot electrons and relieves the hot phonon bottleneck. Plasmon–phonon coupling has been studied extensively in various metal–semiconductor systems.^{60–64} In our nanostructure/ MAPbBr_3 system, relief of this hot phonon bottleneck should also aid in phonon propagation within the active layer, reflected as a decrease in the longer (τ_2) calculated lifetimes (Table 1). It is noteworthy that relative to the reference MAPbBr_3 (0.2 ps), the τ_R of 0.5 wt% Au/Ag NSs (0.09 ps) is more reduced than that of the τ_R of 1.0 wt% Au/Ag NSs (0.15 ps). This indicates that plasmon–phonon coupling is very sensitive to the nanostructure density; at a 1.0 wt% concentration, the sample may have a higher degree of particle aggregation where interparticle coupling likely supersedes plasmon–phonon coupling and results in less relief of the phonon bottleneck.

The amplitude-weighted lifetimes, τ_{avg} , of the PB recovery kinetics at 530 nm significantly decrease with the increasing particle density, from 253 ps for the reference MAPbBr_3 to 167 ps and 104 ps for the 0.5 wt% and 1.0 wt% Au/Ag NSs. A systematic decrease in τ_1 and τ_2 is observed as well. This suggests that the bimetallic nanostructures amplify light trapping in the MAPbBr_3 active layer of PSCs, by both near field coupling of the nanostructures with MAPbBr_3 as well as far field coupling of scattered light into the active layer.^{65–69} The perovskite crystals are exposed to an increased photon flux generated by the intense near fields localized at the sharp edges and corners of vicinal Au/Ag NSs, giving rise to higher carrier densities. The elevated carrier densities are expected to weaken trap-assisted recombination, specifically when the density of charge carriers far exceeds that of the trap states, resulting in shorter carrier lifetimes.⁷⁰ Further the ideal size of these bimetallic nanostructures and the presence of the Ag

layer amplify their ability to scatter light, facilitating enhanced light harvesting and the light is reemitted by the MAPbBr₃ active layer, which improves the optical path length. The enhanced light trapping, in conjunction with improved phonon propagation from relief of the hot phonon bottleneck *via* plasmon–phonon coupling, enhance the number of free carriers generated, which results in more electrons being available to efficiently transfer to the TiO₂ conduction band. This implies that the presence of metal nanostructures leads to faster electron injection into TiO₂, suppressing the recombination in the bulk and resulting in a shorter carrier lifetime as reflected in the TAS results.

To further understand the role of Au/Ag NSs on the carrier dynamics of the MAPbBr₃ films, we supplemented our proposed mechanisms by measuring the steady-state PL and trPL of the reference and plasmon-enhanced films. The MAPbBr₃ reference films exhibited a narrow photoluminescence peak centered around the bandgap (Fig. 5a) of MAPbBr₃ analogous to that demonstrated in the literature.^{71,72} In the presence of the nanostructures, a significant reduction in the PL intensity is observed; where the PL is quenched by ~32% and ~65% with 0.5 wt% and 1.0 wt% silica-coated Au/Ag NSs, respectively. This quenching in steady-state PL indicates that non-radiative decay pathways are favored with the increasing nanostructure density, which decreases exciton decay by recombination and suppression of PL.^{32,73} Our result suggests that the presence of the nanostructures promotes more efficient charge carrier extraction at MAPbBr₃ and mp-TiO₂ interfaces, attributable to the intense electric fields generated by the nanostructures.^{28,74} Furthermore, the enhanced non-radiative decay pathways in the presence of the nanostructures also facilitate below band gap energy transfer into the nearby semi-

conductor, specifically plasmon resonant energy transfer (PRET). PRET, which has been extensively studied in a range of solar energy conversion systems,¹⁹ occurs when the energy localized in plasmon oscillations around the nanostructure is transferred to surrounding semiconductor and induces charge separation and carrier generation.^{19,75,76} PRET does not involve direct electron injection into the semiconductor and is not limited by band alignment or the presence of thin insulating interlayers; therefore the quenching in steady-state PL may reflect resonant energy transfer from the dipole–dipole relaxation of excited plasmons in the nanostructures into both the mp-TiO₂ and MAPbBr₃ crystals. In addition to PRET, hot electron transfer (HET) is another non-radiative enhancement mechanism that occurs when plasmons decay *via* energetic relaxation and create hot electron/hole pairs.^{77,78} These hot electrons can gain enough energy to overcome the Schottky barrier at metal/semiconductor interfaces and inject directly into the semiconductor conduction band.¹⁹ However, we do not anticipate any HET in our system due to the presence of ~5 nm silica insulating layer coating the nanostructures (Fig. 1c); since the electron tunneling barrier of silica is <3 nm,^{79–81} this will prohibit HET from the nanostructures to the perovskite.

The trends in steady-state PL follow the PL decay observed with room temperature trPL measurements of the reference MAPbBr₃ and nanostructure-incorporated films (Fig. 5b). Carrier lifetimes, shown in Table 2, were obtained by fitting the experimental data with a biexponential decay function. The average PL lifetime, τ_{avg} , of the reference films decreased from 2.84 ns to 1.3 ns for the 0.5 wt% Au/Ag NSs and 0.36 ns for the 1.0 wt% Au/Ag. The reduced PL lifetimes correspond well with the quenching in steady-state PL of MAPbBr₃ in the presence of bimetallic nanostructures, which supports our earlier hypothesis of rapid charge transfer and reduced recombination at the plasmon/perovskite interface, enhancing carrier extraction from the MAPbBr₃ to TiO₂. Furthermore, plasmonic nanostructures also decrease the exciton binding energy (E_B) of perovskites; in our system the reduced E_B of MAPbBr₃ by bimetallic nanostructures would also manifest as suppressed PL if charge transfer is promoted into the mp-TiO₂ prior to exciton recombination in the bulk. While the exact mechanism that decreases the E_B of perovskites in the presence of plasmonic nanostructures is not fully understood, it opens up an exciting avenue for MAPbBr₃-based devices, whose enhanced environmental stability relative to MAPbI₃ is offset in part by its higher E_B . Overall, quenching of the steady-state PL and decreases in trPL carrier lifetimes translate well to the increased efficiencies observed for the nanostructure-incorporated PSCs (Fig. 2 and S4†).⁴⁵

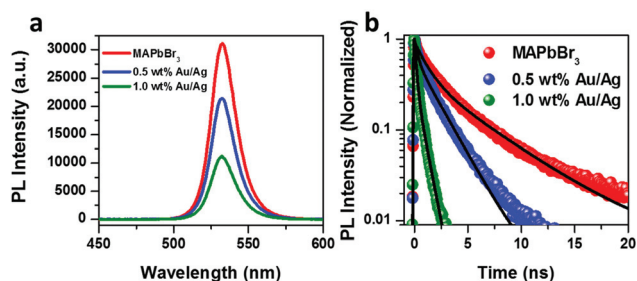


Fig. 5 (a) Steady-state photoluminescence spectra of mesoporous TiO₂ films infiltrated with MAPbBr₃ and different concentrations of silica-coated Au/Ag NSs. (b) The corresponding photoluminescence decay plots of the same samples with 400 nm excitation. Experimental data in (b) are denoted by symbols and have been fitted with a biexponential decay function (black lines).

Table 2 Amplitudes (A), time constants (τ), and amplitude-weighted lifetimes (τ_{avg}) derived from biexponential fits of trPL transients of each sample

Sample	A_1	τ_1 [ns]	A_2	τ_2 [ns]	τ_{avg} [ns]
MAPbBr ₃	0.57 ± 0.01	1.18 ± 0.02	0.40 ± 0.01	5.25 ± 0.05	2.84
0.5 wt% Au/Ag	0.49 ± 0.00	0.31 ± 0.01	0.64 ± 0.00	2.05 ± 0.01	1.30
1.0 wt% Au/Ag	0.77 ± 0.04	0.21 ± 0.01	0.27 ± 0.03	0.79 ± 0.02	0.36

Conclusions

In summary, we boosted the efficiency of MAPbBr₃-based PSCs by incorporating silica-coated Au/Ag bimetallic nanostructures into the mesoporous TiO₂ active layer. The increased light harvesting in the devices as determined by absorbance and IPCE measurements in conjunction with improvements in J_{sc} , V_{oc} , and FF for plasmon-enhanced samples demonstrate strong coupling between Au/Ag NSs and the MAPbBr₃-infiltrated TiO₂ active layer. Our results indicate enhanced carrier generation with decreased recombination in the perovskite in the presence of the nanostructures. The decreased carrier lifetimes obtained from both TAS and trPL measurements and the quenching observed in ssPL further support our hypothesis. Lifetimes obtained from photobleach formation and recovery in transient absorption spectra suggest that the presence of the nanostructures coupled with the MAPbBr₃ improves the hot carrier thermalization to an equilibrium distribution *via* plasmon-phonon coupling. Decreases in lifetimes correlating with electron injection suggest that the presence of Au/Ag NS enhances photoinduced carrier generation as a result of both strong near field and far field coupling of light, promoting efficient electron injection into TiO₂ prior to bulk recombination. Quenching of steady state PL and decreases in carrier lifetimes obtained from trPL, attributed in part to PRET effects and reduction in E_B , provide further evidence to the improved carrier injection in plasmon-enhanced mesoporous perovskites. We envision that these bimetallic nanostructures can be straightforwardly translated to other perovskite systems to enhance the efficiencies not only of solar devices, but also of photodetectors and lasers.

Acknowledgements

HFZ acknowledges support from Vanderbilt University Discovery grant, NSF EPSCOR (NSF EPS1004083), NSF BRIGE (EEC 1342185), and the Department of Education for Graduate Assistance in Areas of National Need (GAANN) Fellowship under grant number P0200A090323. EMT acknowledges the VINSE fellowship and Vanderbilt start-up funds. TEM images were obtained with an instrument supported by NSF EPS 1004083. Ultrafast and photoluminescence measurements were conducted at the Center for Nanophase Materials Sciences, which is a DOE Office of Science User Facility.

References

- 1 M. A. Green, K. Emery, Y. Hishikawa, W. Warta and E. D. Dunlop, *Prog. Photovoltaics*, 2016, **24**, 3–11.
- 2 A. Kojima, K. Teshima, Y. Shirai and T. Miyasaka, *J. Am. Chem. Soc.*, 2009, **131**, 6050–6051.
- 3 M. M. Lee, J. Teuscher, T. Miyasaka, T. N. Murakami and H. J. Snaith, *Science*, 2012, **338**, 643–647.
- 4 H. S. Kim, C. R. Lee, J. H. Im, K. B. Lee, T. Moehl, A. Marchioro, *et al.*, *Sci. Rep.*, 2012, **2**, 00591.
- 5 C. Zuo, H. J. Bolink, H. Han, J. Huang, D. Cahen and L. Ding, *Adv. Sci.*, 2016, **3**, 1500324.
- 6 Y. Tong, E. Bladt, M. F. Ayguler, A. Manzi, K. Z. Milowska, V. A. Hintermayr, *et al.*, *Angew. Chem., Int. Ed.*, 2016, **55**, 13887–13892.
- 7 S. D. Stranks, G. E. Eperon, G. Grancini, C. Menelaou, M. J. Alcocer, T. Leijtens, L. M. Herz, A. Petrozza and H. J. Snaith, *Science*, 2013, **342**, 341–344.
- 8 G. Xing, N. Mathews, S. Sun, S. S. Lim, Y. M. Lam, M. Gratzel, S. Mhaisalkar and T. C. Sum, *Science*, 2013, **342**, 344–347.
- 9 Y. Han, S. Meyer, Y. Dkhissi, K. Weber, J. M. Pringle, U. Bach, L. Spiccia and Y.-B. Cheng, *J. Mater. Chem. A*, 2015, **3**, 8139–8147.
- 10 J. Yang, B. D. Siempelkamp, D. Liu and T. L. Kelly, *ACS Nano*, 2015, **9**, 1955–1963.
- 11 J. H. Noh, S. H. Im, J. H. Heo, T. N. Mandal and S. I. Seok, *Nano Lett.*, 2013, **13**, 1764–1769.
- 12 X. Zheng, B. Chen, C. Wu and S. Priya, *Nano Energy*, 2015, **17**, 269–278.
- 13 C. Zuo and L. Ding, *Adv. Energy Mater.*, 2016, 1601193.
- 14 N. Kedem, T. M. Brenner, M. Kulbak, N. Schaefer, S. Levchenko, I. Levine, D. Abou-Ras, G. Hodes and D. Cahen, *J. Phys. Chem. Lett.*, 2015, **6**, 2469–2476.
- 15 R. Sheng, A. Ho-Baillie, S. Huang, S. Chen, X. Wen, X. Hao and M. A. Green, *J. Phys. Chem. C*, 2015, **119**, 3545–3549.
- 16 E. M. Talbert, H. F. Zarick, N. J. Orfield, W. Li, W. R. Erwin, Z. R. DeBra, *et al.*, *RSC Adv.*, 2016, **6**, 86947–86954.
- 17 E. Edri, S. Kirmayer, D. Cahen and G. Hodes, *J. Phys. Chem. Lett.*, 2013, **4**, 897–902.
- 18 J. H. Heo, D. H. Song and S. H. Im, *Adv. Mater.*, 2014, **26**, 8179–8183.
- 19 W. R. Erwin, H. F. Zarick, E. M. Talbert and R. Bardhan, *Energy Environ. Sci.*, 2016, **9**, 1577–1601.
- 20 F.-C. Chen, J.-L. Wu, C.-L. Lee, Y. Hong, C.-H. Kuo and M. H. Huang, *Appl. Phys. Lett.*, 2009, **95**, 013305.
- 21 A. P. Kulkarni, K. M. Noone, K. Munechika, S. R. Guyer and D. S. Ginger, *Nano Lett.*, 2010, **10**, 1501–1505.
- 22 W. R. Erwin, C. Hungerford, H. F. Zarick, E. M. Talbert, P. Arora and R. Bardhan, *ACS Omega*, 2016, **1**, 722–729.
- 23 H. F. Zarick, W. R. Erwin, A. Boulesbaa, O. K. Hurd, J. A. Webb, A. A. Puretzky, D. B. Geohegan and R. Bardhan, *ACS Photonics*, 2016, **3**, 385–394.
- 24 H. F. Zarick, O. Hurd, J. A. Webb, C. Hungerford, W. R. Erwin and R. Bardhan, *ACS Photonics*, 2014, **1**, 806–811.
- 25 J. Qi, X. Dang, P. T. Hammond and A. M. Belcher, *ACS Nano*, 2011, **5**, 7108–7116.
- 26 M. D. Brown, T. Suteewong, R. S. Kumar, V. D’Innocenzo, A. Petrozza, M. M. Lee, U. Wiesner and H. J. Snaith, *Nano Lett.*, 2011, **11**, 438–445.
- 27 S. Chang, Q. Li, X. Xiao, K. Y. Wong and T. Chen, *Energy Environ. Sci.*, 2012, **5**, 9444–9448.
- 28 Z. Lu, X. Pan, Y. L. Ma, Y. L. Zheng, D. Zhang, Q. Xu, *et al.*, *RSC Adv.*, 2015, **5**, 11175–11179.
- 29 W. Zhang, M. Saliba, S. D. Stranks, Y. Sun, X. Shi, U. Wiesner and H. J. Snaith, *Nano Lett.*, 2013, **13**, 4505–4510.

- 30 H. Yu, J. Roh, J. Yun and J. Jang, *J. Mater. Chem. A*, 2016, **4**, 7322–7329.
- 31 S. Carretero-Palacios, M. E. Calvo and H. Miguez, *J. Phys. Chem. C*, 2015, **119**, 18635–18640.
- 32 M. Saliba, W. Zhang, V. M. Burlakov, S. D. Stranks, Y. Sun, J. M. Ball, *et al.*, *Adv. Funct. Mater.*, 2015, **25**, 5038–5046.
- 33 W. Niu, L. A. Ibbotson, D. Leipold, E. Runge, G. V. Prakash and J. J. Baumberg, *Phys. Rev. B*, 2015, **91**, 161303.
- 34 C. Burda, X. Chen, R. Narayanan and M. A. El-Sayed, *Chem. Rev.*, 2005, **105**, 1025–1102.
- 35 K. L. Kelly, E. Coronado, L. L. Zhao and G. C. Schatz, *J. Phys. Chem. B*, 2003, **107**, 668–677.
- 36 J. A. Schuller, E. S. Barnard, W. Cai, Y. C. Jun, J. S. White and M. L. Brongersma, *Nat. Mater.*, 2010, **9**, 193–204.
- 37 S. Link and M. A. El-Sayed, *Int. Rev. Phys. Chem.*, 2000, **19**, 409–453.
- 38 H. F. Zarick, W. R. Erwin, J. Aufrecht, A. Coppola, B. R. Rogers, C. L. Pint and R. Bardhan, *J. Mater. Chem. A*, 2014, **2**, 7088–7098.
- 39 W. R. Erwin, A. Coppola, H. F. Zarick, P. Arora, K. J. Miller and R. Bardhan, *Nanoscale*, 2014, **6**, 19–22.
- 40 M. Kulbak, D. Cahen and G. Hodes, *J. Phys. Chem. Lett.*, 2015, **6**, 2452–2456.
- 41 J. Burschka, N. Pellet, S. J. Moon, R. Humphry-Baker, P. Gao, M. K. Nazeeruddin and M. Gratzel, *Nature*, 2013, **499**, 316–319.
- 42 C.-C. Chung, C. S. Lee, E. Jokar, J. H. Kim and E. W.-G. Diao, *J. Phys. Chem. C*, 2016, **120**, 9619–9627.
- 43 T. Salim, S. Sun, Y. Abe, A. Krishna, A. C. Grimsdale and Y. M. Lam, *J. Mater. Chem. C*, 2015, **3**, 8943–8969.
- 44 S. Carretero-Palacios, A. Jiménez-Solano and H. Miguez, *ACS Energy Lett.*, 2016, **1**, 323–331.
- 45 J. Cui, C. Chen, J. Han, K. Cao, W. Zhang, Y. Shen and M. Wang, *Adv. Sci.*, 2016, **3**, 1500312.
- 46 B. Cai, Y. Peng, Y. B. Cheng and M. Gu, *Opt. Express*, 2015, **23**, A1700–A1706.
- 47 S. S. Mali, C. S. Shim, H. Kim, P. S. Patil and C. K. Hong, *Nanoscale*, 2016, **8**, 2664–2677.
- 48 R. Wu, B. Yang, C. Zhang, Y. Huang, Y. Cui, P. Liu, *et al.*, *J. Phys. Chem. C*, 2016, **120**, 6996–7004.
- 49 Y. Zhai, C. X. Sheng, C. Zhang and Z. V. Vardeny, *Adv. Funct. Mater.*, 2016, **26**, 1617–1627.
- 50 T. C. Sum, N. Mathews, G. Xing, S. S. Lim, W. K. Chong, D. Giovanni and H. A. Dewi, *Acc. Chem. Res.*, 2016, **49**, 294–302.
- 51 V. Sharma, S. Aharon, I. Gdor, C. Yang, L. Etgar and S. Ruhman, *J. Mater. Chem. A*, 2016, **4**, 3546–3553.
- 52 X. Deng, X. Wen, S. Huang, R. Sheng, T. Harada, T. W. Kee, M. Green and A. Ho-Baillie, *J. Phys. Chem. C*, 2016, **120**, 2542–2547.
- 53 L. Wang, C. McCleese, A. Kovalsky, Y. Zhao and C. Burda, *J. Am. Chem. Soc.*, 2014, **136**, 12205–12208.
- 54 C. S. Ponseca, Y. Tian, V. Sundstrom and I. G. Scheblykin, *Nanotechnology*, 2016, **27**, 082001.
- 55 X. Wu, M. T. Trinh, D. Niesner, H. Zhu, Z. Norman, J. S. Owen, O. Yaffe, B. J. Kudisch and X. Y. Zhu, *J. Am. Chem. Soc.*, 2015, **137**, 2089–2096.
- 56 H. Y. Hsu, C. Y. Wang, A. Fathi, J. W. Shiu, C. C. Chung, P. S. Shen, *et al.*, *Angew. Chem., Int. Ed.*, 2014, **53**, 9339–9342.
- 57 T. C. Sum and N. Mathews, *Energy Environ. Sci.*, 2014, **7**, 2518–2534.
- 58 M. B. Price, J. Butkus, T. C. Jellicoe, A. Sadhanala, A. Briane, J. E. Halpert, *et al.*, *Nat. Commun.*, 2015, **6**, 8420.
- 59 Y. Yang, D. P. Ostrowski, R. M. France, K. Zhu, J. v. d. Lagemaat, J. M. Luther and M. C. Beard, *Nat. Photonics*, 2016, **10**, 53–59.
- 60 S. Das Sarma, J. K. Jain and R. Jalabert, *Phys. Rev. B*, 1988, **37**, 6290–6296.
- 61 E. H. Hwang, R. Sensarma and S. Das Sarma, *Phys. Rev. B*, 2010, **82**, 195406.
- 62 A. A. Kukharskii, *Solid State Commun.*, 1973, **13**, 1761–1765.
- 63 W. Zhao, Q. Wu, Q. Hao, J. Wang, M. Li, Y. Zhang, K. Bi, Y. Chen and Z. Ni, *Appl. Phys. Lett.*, 2016, **108**, 131903.
- 64 X. Zhu, W. Wang, W. Yan, M. B. Larsen, P. Boggild, T. G. Pedersen, S. Xiao, J. Zi and N. A. Mortensen, *Nano Lett.*, 2014, **14**, 2907–2913.
- 65 K.-S. Lee and M. A. El-Sayed, *J. Phys. Chem. B*, 2006, **110**, 19220–19225.
- 66 N. K. Grady, N. J. Halas and P. Nordlander, *Chem. Phys. Lett.*, 2004, **399**, 167–171.
- 67 P. B. Johnson and R. W. Christy, *Phys. Rev. B: Solid State*, 1972, **6**, 4370–4379.
- 68 K. M. Mayer and J. H. Hafner, *Chem. Rev.*, 2011, **111**, 3828–3857.
- 69 J. M. Pitarke, V. M. Silkin, E. V. Chulkov and P. M. Echenique, *Rep. Prog. Phys.*, 2007, **70**, 1–87.
- 70 Z.-Y. Zhang, H.-Y. Wang, Y.-X. Zhang, Y.-W. Hao, C. Sun, Y. Zhang, B.-R. Gao, Q.-D. Chen and H.-B. Sun, *Sci. Rep.*, 2016, **6**, 27286.
- 71 D. Shi, H. Tsai, R. Asadpour, J.-C. Blancon, A. J. Neukirch, G. Gupta, *et al.*, *Science*, 2015, **347**, 519–522.
- 72 V. A. Hintermayr, A. F. Richter, F. Ehrat, M. Doblinger, W. Vanderlinden, J. A. Sichert, *et al.*, *Adv. Mater.*, 2016, **28**, 9478–9485.
- 73 J. Dai, H. Zheng, C. Zhu, J. Lu and C. Xu, *J. Mater. Chem. C*, 2016, **4**, 4408–4413.
- 74 Z. Li, P. P. Boix, G. Xing, K. Fu, S. A. Kulkarni, S. K. Batabyal, *et al.*, *Nanoscale*, 2016, **8**, 6352–6360.
- 75 J. Li, S. K. Cushing, F. Meng, T. R. Senty, A. D. Bristow and N. Wu, *Nat. Photonics*, 2015, **9**, 601–607.
- 76 F. Nan, S. J. Ding, L. Ma, Z. Q. Cheng, Y. T. Zhong, Y. F. Zhang, *et al.*, *Nanoscale*, 2016, **8**, 15071–15078.
- 77 F. B. Atar, E. Battal, L. E. Aygun, B. Daglar, M. Bayindir and A. K. Okyay, *Opt. Express*, 2013, **21**, 7196–7201.
- 78 C. Clavero, *Nat. Photonics*, 2014, **8**, 95–103.
- 79 B. E. Deal and E. H. Snow, *J. Phys. Chem. Solids*, 1966, **27**, 1873–1879.
- 80 C. H. Lin and C. W. Liu, *Sensors*, 2010, **10**, 8797–8826.
- 81 Z. A. Weinberg and A. Hartstein, *Solid State Commun.*, 1976, **20**, 179–182.
- 82 J. A. Webb, W. R. Erwin, H. F. Zarick, J. Aufrecht, H. W. Manning, M. J. Lang, C. L. Pint and R. Bardhan, *J. Phys. Chem. C*, 2014, **118**, 3696–3707.